Geophys. J. Int. (2008) **174,** 941–948 doi: 10.1111/j.1365-246X.2008.03840.x

Cross-dependence of finite-frequency compressional waveforms to shear seismic wave speeds

Zhigang Zhang and Yang Shen

Graduate School of Oceanography, University of Rhode Island, Narragansett, RI 02882, *USA. E-mail: zzhang@gso.uri.edu*

Accepted 2008 April 29. Received 2008 April 28; in original form 2008 March 7

SUMMARY

Seismic tomography has been one of the primary tools to image the interior of the earth and other elastic structures. To date the inversions of compressional (*P*) and shear (*S*) wave speeds have been carried out separately under the assumption that *P* traveltimes are affected only by the *P* wave speed of the elastic media and *S* traveltimes by the *S* wave speed. Using numerical and analytical solutions, we show that for finite-frequency seismic waves, *S* wave speed perturbations may have significant effects on *P* waveforms. This suggests that when waveform-derived traveltime and amplitude anomalies are used in tomographic inversions, the *P*-wave measurements should be related to not only *P* wave speed perturbations but also *S* wave speed perturbations.

Key words: Seismic tomography; Computational seismology; Theoretical seismology; Wave scattering and diffraction; Wave propagation.

INTRODUCTION

For many years, seismologists have made fundamental discoveries about the earth's interior, using rays to describe the propagation of *P* and *S* seismic waves. However, with the increasing need for more accurate images of the earth structure at fine resolution, the limitations of ray theory become problematic. Several recent studies have developed a new theory that describes the sensitivities, or Fréchet kernels, of the traveltimes and amplitudes of finite-frequency seismic waves to perturbations in the properties of wave-propagation media (Dahlen *et al.* 2000; Zhao *et al.* 2000, 2005; Tromp *et al.* 2005). For a finite-frequency wave, the sensitivities to the elastic and anelastic properties are in general distributed in a 3D volume surrounding the ray path. Numerical experiments have demonstrated that, within the limit of Born approximation, the finite-frequency theory represents the propagation of realistic seismic waves more accurately than ray theory when the scales of wave speed heterogeneities are smaller than the Fresnel zones of the waves (Hung *et al.* 2000; Baig *et al.* 2003; Yang & Hung 2005; Zhang *et al.* 2007).

To date the inversions of *P* and *S* wave speeds have been carried out separately under the assumption that *P* traveltimes are affected only by the *P* wave speed of the elastic media and *S* traveltimes by the *S* wave speed (e.g. Dziewonski & Anderson 1984; Grand 1987; Zhao *et al.* 1992; van der Hilst *et al.* 1997). With the approximations of only forward scattering of body wave and far field, Dahlen *et al.* (2000) considered that only *P*-to-*P* scattering off a compressional wave speed heterogeneity and like-type *S*-to-*S* scattering off a shear wave speed heterogeneity are significant. Although several studies have documented the scattering of wave field by an arbitrary heterogeneity (Wu & Aki 1985) and have calculated the sensitivity kernels with the near-field terms or in a full-wave approach (Favier *et al.* 2004; Tromp *et al.* 2005; Zhao *et al.* 2005; Liu & Tromp 2006), the assumption that the propagation of *P* or *S* waves depends solely on the *P* or *S* wave speed structure, respectively, has remained unchanged in the applications of the finite-frequency theory to date (Hung *et al.* 2004; Montelli *et al.* 2006; Yang *et al.* 2006; Chen *et al.* 2007). In this paper, we document the contributions of *S* wave speed perturbations to the *P*-wave traveltimes and amplitude anomalies using numerical and analytical solutions. We conclude that neglecting the cross-dependence between *P* waveforms and *S* wave speed perturbations distorts the forward relation between the wave propagation medium and observations and may cause a systematic bias in the solution of *P* wave speeds.

MODELS AND RESULTS

To demonstrate the cross-dependence of *P* and *S* waveforms and wave speed perturbations, we carry out numerical experiments using a 3-D staggered-grid, finite-difference method (Olsen 1994). We use a simple homogenous model as our reference model, so the results can be compared to and also analysed with the analytical solutions. The *P* and *S* wave speeds in the reference model are 6.5 and 3.5 km s^{-1}, respectively. The grid spacing is 200 m, and the time step 0.01 s. We introduce a cylindrical-shaped velocity perturbation with a radius of 3 km, a height of 6 km at various depths along a vertical line between the source and receiver, the axis of which is always oriented vertically in the *Z* direction (Fig. 1). The traveltime and amplitude anomalies caused by the wave speed perturbation are measured by cross-correlation of the waveforms with and without the wave speed perturbation. For simplicity, an explosive source with a dominant period of 1.2 *s* is used to observe the direct *P* arrival. When only the *P* or *S* wave speed is perturbed, the sensitivities to the *P* or *S* wave speed perturbations (Fig. 2) calculated using the scattering-integral method (Appendix A) predict

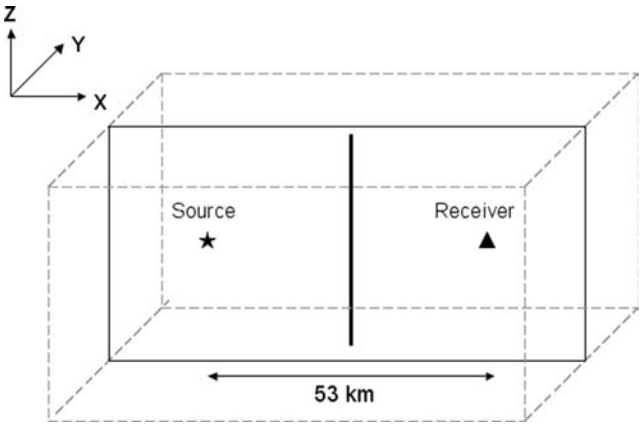

Figure 1. The geometry of the homogeneous and isotropic model used in the numerical simulations. The rectangle with solid lines shows the vertical cross-section of the model containing the source (star) and receiver (triangle). The horizontal distance from the source to the receiver is 53 km, or approximately 7.4 wavelengths of the dominant *P* wave. The vertical line in between the source and receiver shows where a cylindrical-shaped wave speed anomaly is placed.

the *P* traveltime and amplitude anomalies that accurately match the direct waveform cross-correlation measurements (Fig. 3). Since the density remains the same in all the calculations, a perturbation in only the *P* wave speed is equivalent to a perturbation in the bulk modulus, while a perturbation in only the *S* wave speed corresponds to changes in both the bulk and shear moduli. When both the *P* and *S* wave speeds are perturbed within the cylindrical anomaly, however, the predicted *P* traveltime and amplitude anomalies from the sensitivities to *P* wave speed perturbations alone do not match the direct waveform cross-correlation measurements (Fig. 3). Only after we add the contributions from the sensitivities of the *P* arrival to *S* wave speed perturbations, do the kernel predictions match the values from the direct waveform cross-correlation, indicating that *S* wave speed perturbations affect the *P* arrival. On the other hand, *P* wave speed perturbations have little effect on the direct *S* arrival in the experiment using a double-couple source to generate *S* waves (Fig. 3).

The sensitivities of *P* traveltime to *P* wave speed perturbations ($K^P_{\alpha,p}$, Fig. 2) are similar to the classic 'banana—doughnut' kernels of Dahlen *et al.* (2000), with a minimum sensitivity along the ray path, though in this study the ray path is a straight line and the kernels are calculated from the full wavefield. In contrast, the sensitivities of *P* traveltime to *S* wave speed perturbations are at the maximum along the ray path ($K^P_{\beta,p}$). The patterns of the sensitivities for *P* amplitude variation to *P* and *S* wave speed perturbations are also reversed: the maximum amplitude sensitivities along the ray path for *P* wave speed perturbations ($K^P_{\alpha,q}$) and minimum sensitivities along the ray path for *S* wave speed perturbations ($K^P_{\beta,q}$).

In a homogeneous and isotropic medium, as in the above numerical experiments, the sensitivity kernels to *P* and *S* wave speed perturbations can also be calculated from the analytical wavefield solutions (Aki & Richards 2002) and the results confirm the finite-difference calculations. Using various combinations of the near- and far-field terms for the source and receiver, we find that both the far- and near-field terms from the source and receive contribute to the *P* traveltime and amplitude sensitivities to *S* wave speed perturbations. In particular, the near- and mid-field terms are mainly responsible for the sensitivities along the ray path (more in the following section). Furthermore, the ratio of the maximum, absolute traveltime sensitivities to *S* wave speed and *P* wave speed perturbations ($K^P_{\beta,p}/K^P_{\alpha,p}$) is approximately $4\lambda_P\beta^2/(l\alpha^2)$ at the mid point between the source and receiver, where λ_P is the wavelength of the *P* wave, l the source–receiver distance, α the *P* wave speed, and β the *S* wave speed. Using the parameters in our numerical experiments (Fig. 1), we find a ratio of about 0.17, consistent with the sensitivity kernels (Fig. 2) and direct waveform cross-correlation measurements (Fig. 3).

Although a homogeneous and isotropic medium is an oversimplification of the real Earth, the above formula for the relative magnitude of the sensitivities to *P* and *S* wave speed perturbations provides a simple way to assess, to the first order, the condition under which the contributions of *S* wave speed perturbations to *P* waveforms are nontrivial. For a medium with a α/β of 1.7–2.0, a value suitable for most of the solid earth, the ratio of the maximum traveltime sensitivities to *S* wave speed and *P* wave speed perturbations at the mid point between the source and receiver decreases from ∼0.17 for a source–receiver geometry with l/λ_P of ∼7.4 to ∼0.017 for a *P* wave of the same wavelength at 10 times the propagation distance ($l/\lambda_P = 74$).

To assess the global relative contributions of *P* and *S* wave speed perturbations to *P* traveltimes and amplitudes, we integrate the absolute values of the sensitivities over the entire volume. For *P*-wave traveltimes, the ratio of the integrated absolute values ($K^P_{\beta,p}/K^P_{\alpha,p}$) varies from 4.1 per cent at l/λ_P of ∼600 to 31 per cent at l/λ_P of ∼7 (Fig. 4). For *P*-wave amplitude anomalies, the ratio of the integrated absolute values ($K^P_{\beta,q}/K^P_{\alpha,q}$) changes from 2.7 to 49 per cent at the same corresponding distances.

DISCUSSION

In the above calculations, the magnitude of *S* wave speed perturbations is the same as the magnitude of *P* wave speed perturbations. In the real Earth, *S* wave speed variations are usually larger than *P* wave speed variations in percentage (e.g. Karato & Karki 2001). One per cent of partial melt in the upper mantle, for example, is estimated to cause 3.6 per cent *P* wave speed reduction and 7.9 per cent *S* wave speed reduction (Hammond & Humphreys 2000). The net effect of a larger *S* wave speed perturbation than the *P* wave speed change is an increase of the contribution and importance of *S* wave speed variations to *P* waveforms. *P* and *S* wave speed variations are also often coupled in the real earth. In such a case, a small-scale perturbation along the ray path affects *P* waveforms when both *P* and *S* wave speeds are taken into consideration. This proves to be important in the numerical validation of the sensitivity kernels (Fig. 3).

Separating the far-field term (with $1/r$ decay, where r is the distance to the source or receiver) from the mid- and near-field terms (with $1/r^2$ decay and $1/r^3$ decay, respectively) in the analytical solution of a homogeneous and isotropic medium (Aki & Richards 2002), we find that the sensitivities of *P* traveltime to *P* wave speed perturbations calculated from the far-field alone are the same as the 'banana–doughnut' kernels of Dahlen *et al.* (2000), with a zero traveltime sensitivity along the ray path (Fig. 5). The far-field *P* traveltime sensitivity to *S* wave speed perturbations is also zero along the ray path. However, off the ray path the sensitivity is nontrivial compared to the sensitivity to *P* wave speed perturbations (Fig. 5). Unlike the scattering of a *P* wave by a *P* wave speed perturbation, the far-field Rayleigh scattering coefficient of a scattered *P* wave due to an *S* wave speed perturbation is zero on the ray path (fig. 4

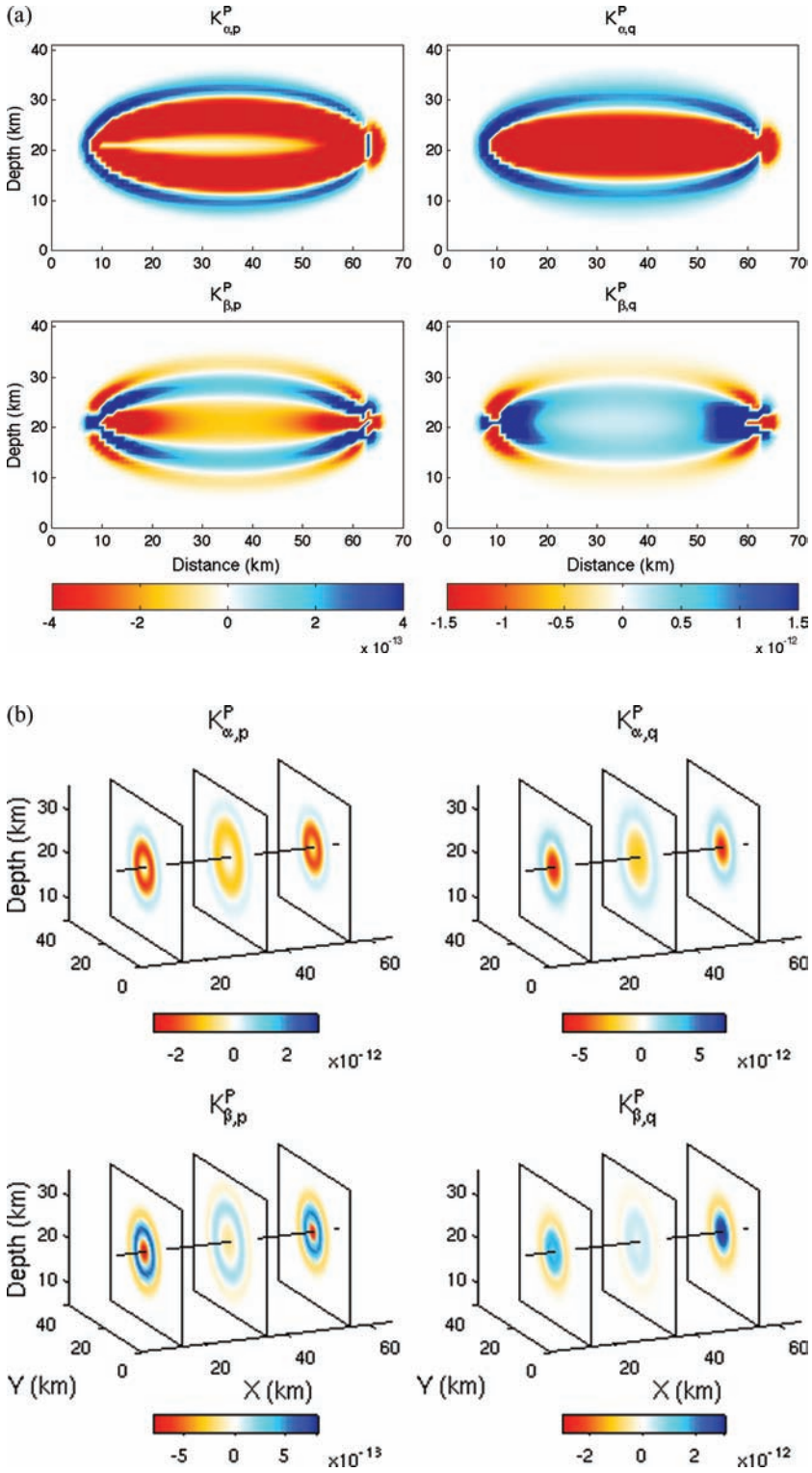

Figure 2. (a) The sensitivity kernels for the horizontal component of the direct *P* arrival in the vertical plane containing the source and receiver. $K^P_{\alpha,p}$ and $K^P_{\alpha,q}$ are the traveltime and amplitude sensitivity kernels to *P* wave speed perturbations, respectively; $K^P_{\beta,p}$ and $K^P_{\beta,q}$ are the traveltime and amplitude sensitivities to *S* wave speed perturbations, respectively. The unit of the traveltime sensitivity is s m^{-3} and that of the amplitude sensitivity is 1 m^{-3} (Zhang *et al.* 2007). (b) The $K^P_{\alpha,p}$, $K^P_{\alpha,q}$, $K^P_{\beta,p}$ and $Ks^P_{\beta,q}$ sensitivities at three vertical planes perpendicular to the ray path. The black line crossing the three planes represents the ray path. The source is located at the left-hand side of this figure. The three planes are 6.5, 26.5 and 46.5 km away from the source, respectively. Less saturated and different colour scales are used to illustrate the details of the kernels.

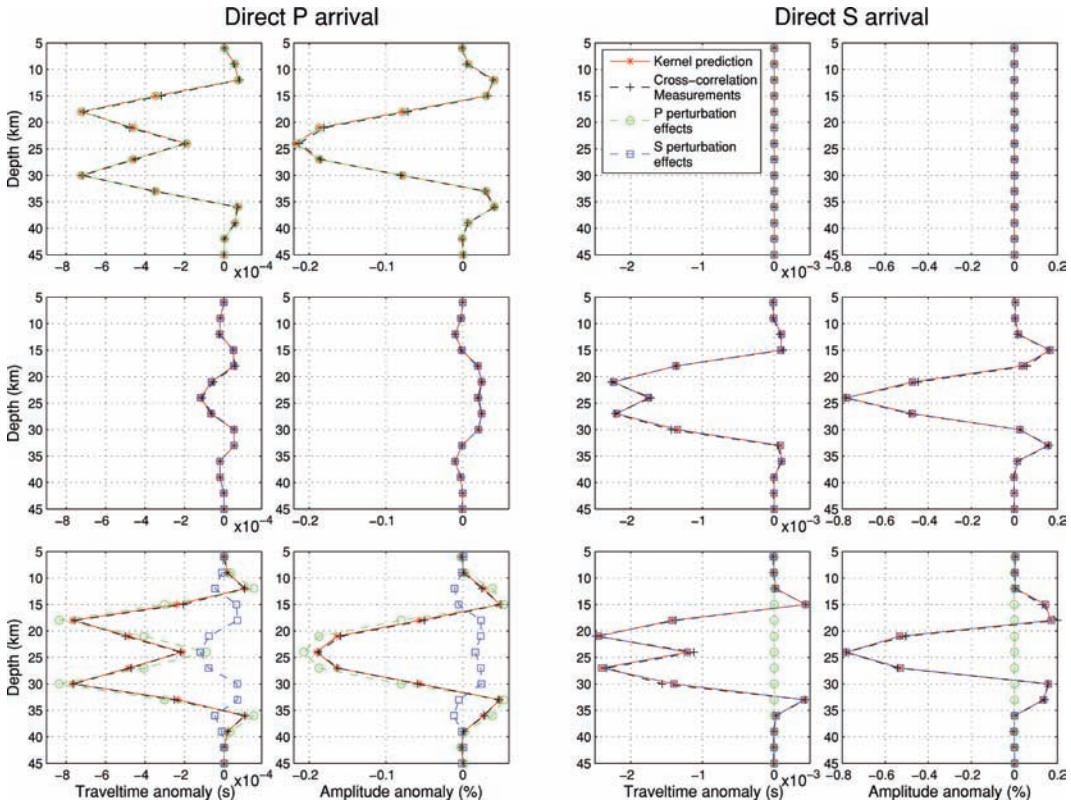

Figure 3. The waveform cross-correlation measurements of the traveltime and amplitude anomalies caused by the cylindrical-shaped wave speed perturbation are compared to the predicted values from the sensitivity kernels. The horizontal axes are traveltime or amplitude anomaly, and the vertical axes are the depth of the centre of the cylindrical-shaped wave speed perturbation along the vertical line between the source and receiver in Fig. 1. The left-hand panels are for the direct *P* arrival. The right-hand panels are for the direct *S* arrival when a double couple source is used. The top row is for the model with only *P* wave speed perturbations (a square cosine function with the 3 per cent maximum at the centre of the perturbation and zeros at the boundaries), the middle row for the model with only *S* wave speed perturbations of the same magnitude, and the bottom row for the model with both *P* and *S* wave speed perturbations (3 per cent uniform).

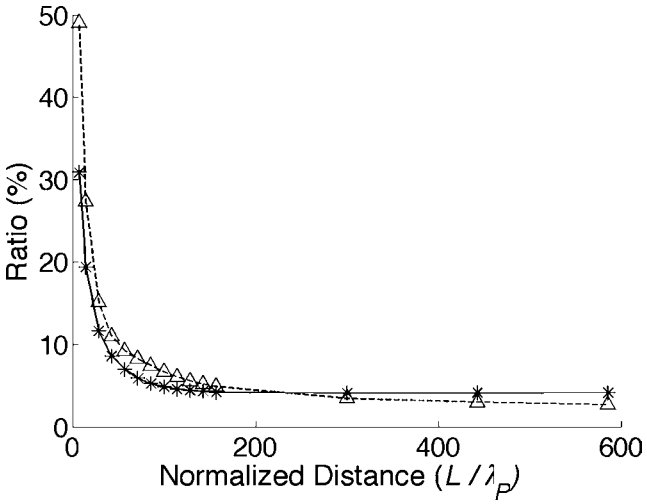

Figure 4. The relative magnitudes of the integrated absolute *P* traveltime (asterisk) and amplitude (triangle) sensitivities to *S* and *P* wave speed perturbations vary with the normalized distance between the source and receiver. The *P* and *S* wave speeds of the medium and the source time function are the same as in the numerical experiment (Fig. 1). At one wavelength distance, the ratios are 110 per cent for traveltime and 540 per cent for amplitude (off scale).

in Dahlen *et al.* 2000). This causes a noticeably wider 'doughnut' hole in $K^P_{\beta,p}$ compared to that of $K^P_{\alpha,p}$.

Keeping the far-field term on the source side but including also the near- and mid-field terms on the receiver side results in the *P* traveltime sensitivity to *S* wave speed perturbations along the ray path, with the most significant change on the receiver side (Fig. 6). The change of $K^P_{\beta,p}$ from the zero sensitivity along the ray path in the case with only the far-field term (Fig. 5) to the local maximum sensitivity in Fig. 6 is attributed to two factors. First, the scattering coefficient for a mid-field scattered *P* wave due to an *S* wave speed perturbation is the maximum along the ray path (Aki & Richards 2002; Favier *et al.* 2004). Second, the mid-field term of a scattered wave is proportional to the time derivative of the reference displacement at the receiver (Aki & Richards 2002). For such a perturbed waveform, the delay time calculated by eq. (A1) in Appendix A is the maximum when there is no offset in the arrival times of the reference and scattered waves (in other word, when the scatter is on the ray path).

Replacing the far-field term on the source side with the near- and mid-field terms while keeping the full terms on the receiver side reveals that the near- and mid-field terms on the source side also contribute to the *P* traveltime sensitivity to *S* wave speed perturbations along and near the ray path, with a stronger sensitivity near the source (Fig. 7).

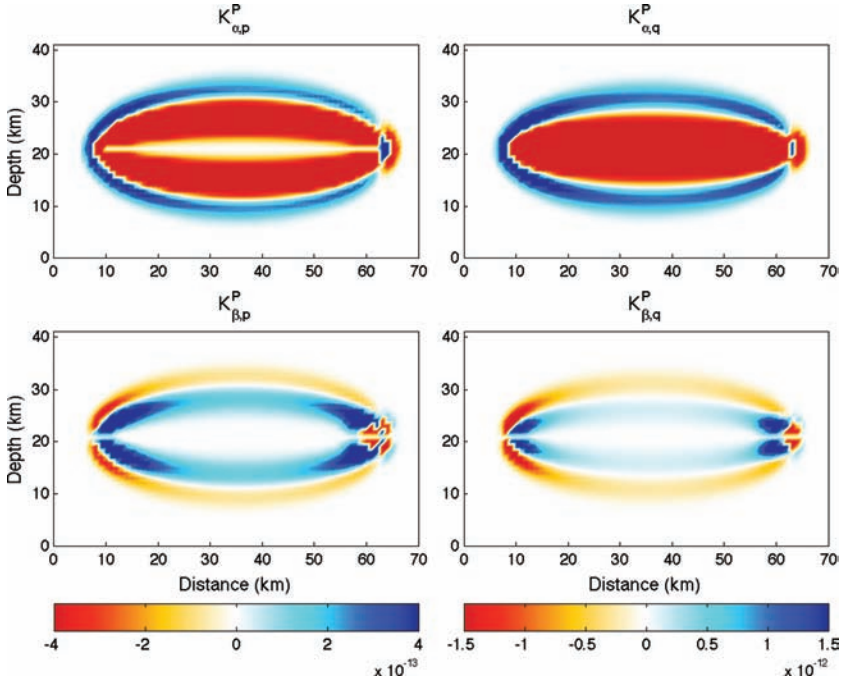

Figure 5. Far-field *P* traveltime and amplitude sensitivity kernels to *P* (top panels) and *S* (bottom panels) wave speed perturbations in the vertical plane containing the source and receiver. The units of the sensitivities are the same as in Fig. 2.

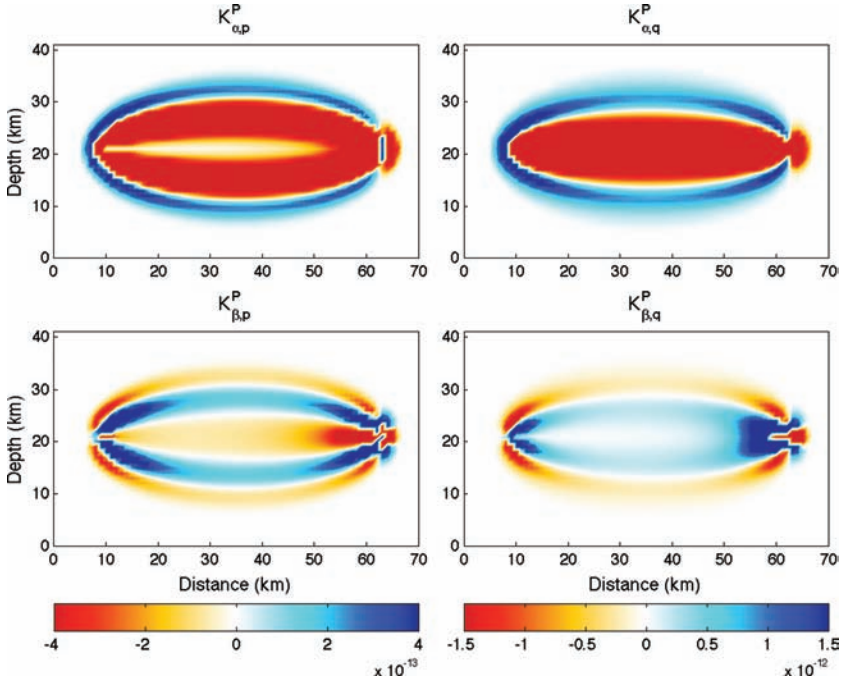

Figure 6. The *P* traveltime and amplitude sensitivity kernels to *P* (top panels) and *S* (bottom panels) wave speed perturbations are calculated with the contributions from the far-field term on the source side and all the field terms on the receiver side. The vertical cross-section contains the source and receiver and the units of the sensitivities are the same as in Fig. 2.

We note the sensitivity to *S* wave speed perturbations oscillates from negative to positive values away from the ray path (Figs 2, 3 and 6). Unlike the sensitivity to *P* wave speed perturbations, integration of the sensitivity to *S* wave speed perturbations in a plane perpendicular to the ray path causes the cancellation of the positive and negative values. A uniform *S* wave speed perturbation in a plane perpendicular to the ray path yields no travel time anomaly in the *P* arrival. This means that *S* wave speed perturbations that are much larger than the width of the Fresnel zone ($\sim 2\sqrt{\lambda l}$ when $l \gg \lambda$, where l is the distance to the receiver and λ the wavelength, Dahlen *et al.* 2000) contribute little to *P* waveform perturbations. Integrating *P* delay times caused by the near-, mid- and far-field terms in planes perpendicular to the ray path, Favier *et al.* (2004) noted that the far-field term becomes predominant at distances greater than

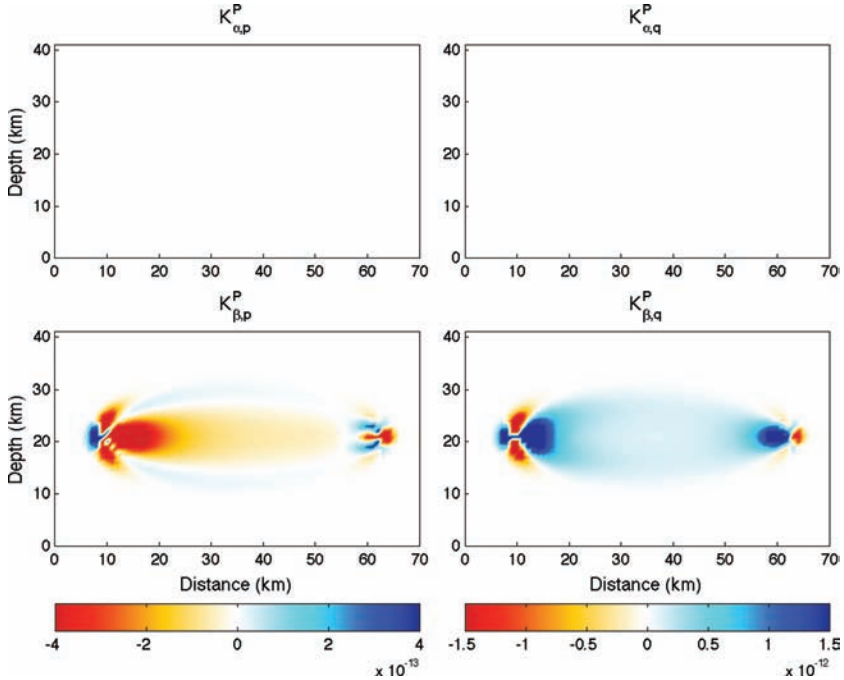

Figure 7. The *P* traveltime and amplitude sensitivity kernels to *P* (top panels) and *S* (bottom panels) wave speed perturbations are calculated with the contributions from the near- and mid-field terms on the source side and all the field terms on the receiver side. The vertical cross-section contains the source and receiver. The units of the sensitivities are the same as in Fig. 2.

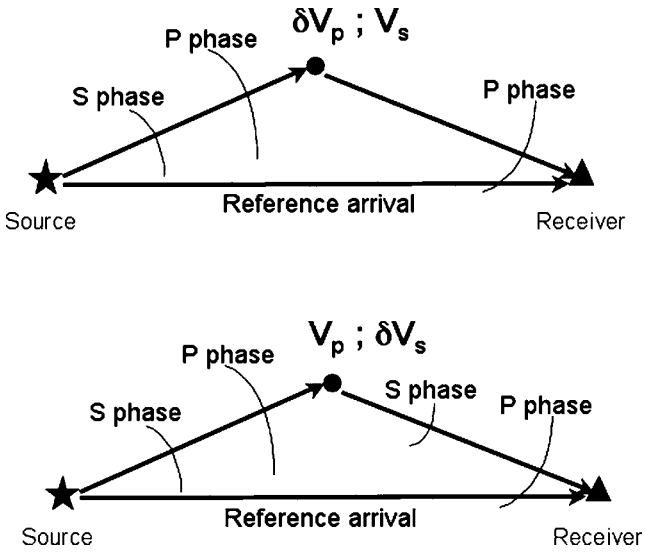

Figure 8. A cartoon illustrating wave propagation due to a scatter. The star represents a source, the triangle a receiver, and the circle a scatter. If only the *P* wave speed is perturbed, only *P* wave is scattered by the scatter (the upper figure). But both *P* and *S* waves are scattered if the *S* wave speed is perturbed (the lower figure).

1/20th wavelength from the receiver and concluded that the mid-field term cannot be neglected at distances within one wavelength from the receiver. However, for heterogeneities on the scale of, and smaller than, the width of the sensitivity kernels (in other words in places where the finite-frequency kernels matter for tomography), the absolute or maximum sensitivities are more meaningful values to assess the relative importance of the finite-frequency kernels to *P* and *S* wave speed perturbations. Fig. 4 shows that the contributions of *S* wave speed perturbations to *P* traveltime and amplitude anomalies are substantial at distances within several tens of wavelengths from the source and receiver. So this cross-dependence of *P* traveltime and amplitude on *S* wave speed is a typical finite-frequency effect, important where the scale of the velocity heterogeneity is comparable or smaller than the Fresnel zone of the wave.

Our results differ from the common practice in tomographic inversion, in which *P*-wave traveltimes depend only on *P* wave speed and *S*-wave traveltimes only on *S* wave speed. This common practice may stem from two well-known theoretical derivations: the Helmholtz poterntial decomposition in a homogenous isotropic mediaum, and ray theory, in which the spatial gradients of the elastic properties are neglected under the high-frequency approximation (e.g. Dahlen & Tromp 1998; Aki & Richards 2002). The effects of *S* wave speed perturbations on *P* waveforms presented in this paper result from the terms neglected by ray theory. For general elastic media, the spatial gradients of the elastic properties result in a scalar (*P*) wave potential that explicitly depends on the spatial gradient of the *S* wave speed (Appendix B). The finite-frequency kernels quantitatively reflect that there is only scattered *P* wave when only *P* wave speed is perturbed. But an *S* wave speed perturbation generates both scattered *P* and *S* wave (Fig. 8).

Although the reference model used in this paper is an isotropic and homogeneous medium, the spatial gradient in the elastic properties must be considered once a wave speed perturbation is introduced into the medium. The numerical approach shown in Fig. 2 can be applied to any general inhomogeneous media, in which the finite-frequency phenomena documented in this paper should also exist.

CONCLUSIONS

For finite-frequency waves, *S* wave speed perturbations may have significant effects on *P* waveforms. Whether this cross-dependence is small enough to be neglected depends on the scale of wave speed

heterogeneities in the Earth and achievable resolution in specific studies. At short source–receiver distances (Fig. 4) and near the source and receiver, the cross-dependence of *P* waveforms on *S* wave speed is substantial. This has important implications for seismic tomography, particularly for regional teleseismic tomography and local earthquake tomography, in which the volume of interest is often within several 10s of wavelength from receivers or both sources and receivers. Even for regions far from sources and receivers, neglecting this cross-dependence means that the estimate of the *P* wave speed near the source (e.g. subduction zone) and receiver is likely biased and such errors may propagate into the rest of the model in tomographic inversions. When the goal of tomographic inversion is to place constraints on thermal and compositional variations in the crust and mantle, the cross-dependence of *P* waveforms on *S* wave speed variations documented above becomes important and requires a joint solution of both the *P* and *S* wave speed structures.

ACKNOWLEDGMENTS

Kim Olsen provided the finite-difference waveform simulation code used in the waveform simulation. We thank Wei Zhang and Li Zhao for discussions, Po Chen and an anonymous reviewer for constructive reviews. This work was supported by Air Force Research Laboratory FA8718-06-C-0014 and U.S. National Science Foundation under grant no. 0241655.

REFERENCES

Aki, K. & Richards, P.G., 2002. *Quantitative Seismology,* University Science Books, Sausalito, California.

Baig, A.M., Dahlen, F.A. & Hung, S.-H., 2003. Traveltimes of waves in three-dimensional random media, *Geophys. J. Int.,* **153,** 467–482.

Chen, P., Zhao, L. & Jordan, T.H., 2007. Full 3D tomography for crustal structure of the Los Angeles Region, *Bull. seism. Soc. Am.,* **97**(4), 1094–1120, doi:10.1785/0120060222.

Dahlen, F.A., Nolet, G. & Hung, S.-H., 2000. Fréchet kernels for finite-frequency traveltime. I: theory, *Geophys. J. Int.,* **141,** 157–174.

Dahlen, F.A., & Tromp, J., 1998. *Theoretical Global Seismology,* Princeton University Press, Princeton, New Jersey.

Dziewonski, A.M. & Anderson, D.L., 1984. Seismic tomography of the Earth's interior, *Am. Sci.,* **72,** 483–494.

Favier, N., Chevrot, S. & Komatitsch, D., 2004. Near-field influence on shear wave splitting and traveltime sensitivity kernels, *Geophys. J. Int.,* **156,** 467–482, doi:10.1111/j.1365-246X.2004.02178.x.

Grand, S.P., 1987. Tomographic inversion for shear velocity beneath the North American plate, *J. geophys. Res.,* **92,** 14 065–14 090.

Hung, S.-H., Dahlen, F.A. & Nolet, G., 2000. Frechet kernels for finite-frequency traveltimes—II, Examples. *Geophys. J. Int.,* **141,** 175–203.

Hung, S.-H., Shen, Y., & Chiao, L.-Y., 2004. Imaging seismic velocity structure beneath the Iceland hotspot – A finite frequency approach, *J. geophys. Res.,* **109,** B08305, doi:10.1029/2003JB002889.

Hammond, W. C. & Humphreys, E. D., 2000. Upper mantle seismic wave velocity: Effects of realistic partial melt geometries, *J. geophys. Res.,* **105,** 10 975–10 986.

Karato, S. & Karki, B.B., 2001 Origin of lateral variation of seismic wave velocities and density in the deep mantle, *J. geophys. Res.,* **106,** 21 771–21 783.

Liu, Q. & Tromp, J., 2006. Finite-frequency kernels based on adjoint methods, *Bull. seism. Soc. Am.,* **96,** 2383–2397, doi:10.1785/0120060041.

Montelli, R., Nolet, G., Dahlen, F.A. & Masters, G., 2006. A catalogue of deep mantle plumes: new results from finite-frequency tomography, *Geochem. Geophys. Geosyst.,* **7,** Q11007, doi:10.1029/2006GC001248.

Olsen, K.B., 1994. Simulation of three-dimensional wave propagation in the Salt Lake Basin, *PhD thesis*. University of Utah, Salt Lake City, Utah, 157p.

Tanimoto, T., 1995. Formalism for traveltime inversion with finite frequency effect. *Geophys. J. Int.,* **121,** 103–110.

Tromp, J., Tape, C.H., & Liu, Q., 2005. Seismic tomography, adjoint methods, time reversal, and banana-doughnut kernels, *Geophys. J. Int.,* **160,** 195–216.

Van Der Hilst, R.D., Widyantoro, S. & Engdahl, E.R., 1997. Evidence for deep mantle circulation from global tomography, *Nature,* **386,** 578–584.

Wu, R. & Aki, K., 1985. Scattering characteristics of elastic waves by an elastic heterogeneity, *Geophysics,* **50,** 582–595.

Yang, H.-Y. & Hung, S.-H., 2005. Validation of ray and wave theoretical travel times in heterogeneous random media, *Geophys. Res. Lett.,* **32,** L20302, doi:10.1029/2005GL023501.

Yang, T., Shen, Y., Van Der Lee, S., Solomon, S.C. & Hung, S.-H., 2006. Upper mantle structure beneath the Azores hotspot from finite-frequency seismic tomography, *Earth planet. Sci. Lett.,* **250,** 11–26.

Zhang, Z., Shen, Y. & Zhao, L., 2007. Finite-frequency sensitivity kernels for head waves, *Geophys. J. Int.,* **171,** 847–856, doi:10.1111/j.1365–246X.2007.03575.x.

Zhao, D., Hasegawa, A. & Horiuchi, S., 1992. Tomograhic Imaging of *P* and *S* wave velocity structure beneath northeastern Japan, *J. geophys. Res.,* **97,** 19 909–19 928.

Zhao, L., Jordan, T.H. & Chapman, C.H., 2000. Three-dimensiional Fréchet differential kernels for seismic delay times, *Geophys. J. Int.,* **141,** 558–576.

Zhao, L., Jordan, T.H., Olsen, K.B. & Chen, P., 2005. Fréchet kernels for imaging regional earth structure based on three-dimensional reference models, *Bull. seism. Soc. Am.,* **95**(6), 2066–2080, doi:10.1785/0120050081.

APPENDIX A: CALCULATION OF THE SENSITIVITIES BY THE SCATTERING INTEGRAL METHOD

We define the traveltime and amplitude anomalies, $\delta\tau p$ and δA_q, respectively, as (Tanimoto 1995; Dahlen *et al.* 2000; Zhao *et al.* 2005):

$$\delta\tau_p = -\frac{\int_{t_1}^{t_2} \dot{\tilde{u}}_l(t)\delta u_l(t)\mathrm{d}t}{\int_{t_1}^{t_2} \left|\dot{\tilde{u}}_l(t)\right|^2 \mathrm{d}t} \tag{A1}$$

$$\delta A_q = -\frac{\int_{t_1}^{t_2} \tilde{u}_l(t)\delta u_l(t)\mathrm{d}t}{\int_{t_1}^{t_2} |\tilde{u}_l(t)|^2 \mathrm{d}t}, \tag{A2}$$

where $\tilde{u}_l(t)$ is the displacement calculated from the reference model in the direction $\hat{e}_l$, a unit vector; $\delta u_l(t) = u_l(t) - \tilde{u}_l(t)$; $u_l(t)$; is the displacement for the perturbed velocity model; a dot represent the time derivative; t_1 and t_2 are the upper and lower limit of the time window of the arrival. The amplitude anomaly defined here is different from that in Zhao *et al.* (2005) by a constant. Following the same algebra in Zhao *et al.*

(2005), we have:

$$K_{\alpha,p} = \frac{1}{P_l}\int_{t_1}^{t_2} 2\tilde{\rho}\tilde{\alpha}\dot{\tilde{u}}_l(r_R,t;r_S)\int_{-\infty}^{\infty}\hat{e}_l\cdot[(\nabla\cdot\tilde{G}^T)(\nabla\cdot\tilde{u})]\mathrm{d}\tau\,\mathrm{d}t \tag{A3}$$

$$K_{\alpha,p} = \frac{1}{Q_l}\int_{t_1}^{t_2} 2\tilde{\rho}\tilde{\alpha}\tilde{u}_l(r_R,t;r_S)\int_{-\infty}^{\infty}\hat{e}_l\cdot[(\nabla\cdot\tilde{G}^T)(\nabla\cdot\tilde{u})]\mathrm{d}\tau\,\mathrm{d}t \tag{A4}$$

$$K_{\beta,p} = \frac{1}{P_l}\int_{t_1}^{t_2} 2\tilde{\rho}\tilde{\beta}\dot{\tilde{u}}_l(r_R,t;r_S)\int_{-\infty}^{\infty}\hat{e}_l\cdot\{((\nabla\tilde{G}^{213}):[(\nabla\tilde{u})+(\nabla\tilde{u})^T]-2(\nabla\cdot\tilde{G}^T)(\nabla\cdot\tilde{u})\}\mathrm{d}\tau\,\mathrm{d}t \tag{A5}$$

$$K_{\beta,q} = -\frac{1}{Q_l}\int_{t_1}^{t_2} 2\tilde{\rho}\tilde{\beta}\tilde{u}_l(r_R,t;r_S)\int_{-\infty}^{\infty}\hat{e}_l\cdot\{((\nabla\tilde{G}^{213}):[(\nabla\tilde{u})+(\nabla\tilde{u})^T]-2(\nabla\cdot\tilde{G}^T)(\nabla\cdot\tilde{u})\}\mathrm{d}\tau\,\mathrm{d}t, \tag{A6}$$

where the $\tilde{G}$ is the Green's tensor. The symbol $()^{213}$ represents the transposition of the first and the second indices of a third-order tensor. P_l and Q_l are the normalization factor in the direction $\hat{e}_l$, which are:

$$P_l = \int_{t_1}^{t_2}\left|\dot{\tilde{u}}_l(t)\right|^2\mathrm{d}t \tag{A7}$$

$$Q_l = \int_{t_1}^{t_2}|\tilde{u}_l(t)|^2\,\mathrm{d}t. \tag{A8}$$

For the direct P wave, for example, the sensitivity kernels to P and S wave speed perturbations, $K^P_{\alpha,p}$ and $K^P_{\beta,p}$, are calculated from eq. (A3) and (A5), respectively, with a time window (t_1, t_2) that contains the P arrival.

APPENDIX B: WAVE EQUATION REPRESENTED BY THE HELMHOLTZ POTENTIAL

The cross-dependence of P waveforms to S wave speed perturbations and the lack of effects of P wave speed perturbations to S waveforms can be understood from the elastodynamic equation,

$$\rho\ddot{\vec{u}} = \nabla\cdot\vec{\vec{\sigma}}, \tag{A9}$$

where ρ is density, $\vec{u}$ displacement, and $\vec{\vec{\sigma}}$ stress. For simplicity, the body force term is omitted in the equation. The displacement can be represented by the Helmholtz scalar potential of P wave, ϕ, and the vector potential of S wave, $\vec{\psi}$ (e.g. Aki & Richards 2002),

$$\vec{u} = \nabla\phi + \nabla\times\vec{\psi} \quad \text{with} \quad \nabla\cdot\vec{\psi} = 0. \tag{A10}$$

Using the linear, isotropic stress–strain relationship, taking the divergence and curl of eq. (A9), and assuming a constant density, we have,

$$\nabla^2\ddot{\phi} = \nabla^2(\alpha^2\nabla^2\phi) + 2\nabla\cdot[\nabla\nabla\times\vec{\psi}\cdot\nabla\beta^2 + \nabla\nabla\phi\cdot\nabla\beta^2 - \nabla\beta^2\nabla^2\phi] \tag{A11}$$

$$\nabla\times\nabla\times\ddot{\vec{\psi}} = -\nabla\times\nabla\times[\beta^2\nabla\times\nabla\times\vec{\psi}] + 2\nabla\times[\nabla\nabla\times\vec{\psi}\cdot\nabla\beta^2 + \nabla\nabla\phi\cdot\nabla\beta^2 - \nabla\beta^2\nabla^2\phi]. \tag{A12}$$

While eq. (A11) shows that the P-wave scalar potential ϕ is explicitly related to the P wave speed, α, and the spatial gradient of the S wave speed, β, the S-wave vector potential $\vec{\psi}$ is related only to β in eq. (A12). Although eq. (A12) includes two terms related to ϕ, they have no effect on $\vec{\psi}$, where the spatial gradient in S wave speed is zero or when $\vec{\psi}$ and ϕ are separated in the time domain.